

Internal tides generated on a corrugated continental slope:  
Part 2. Along-slope barotropic forcing

Sonya Legg

Department of Physical Oceanography,  
Woods Hole Oceanographic Institution, Woods Hole, MA 02543  
Submitted to Journal of Physical Oceanography

June 3, 2003

# Abstract

Recent measurements in a region of continental slope characterized by ridges and valleys running up and down the slope reveal interesting high mode structure in the tidal band velocity signals, with enhanced mixing above the corrugations. In order to understand these observations we have performed numerical simulations of the internal tide generation in this region of topography. Here we focus on the response of the flow to along-slope barotropic tidal forcing. For small amplitude barotropic forcing, internal waves are generated over the continental slope which propagate toward the ocean surface, and toward shallower water. When higher amplitude forcing is combined with large amplitude corrugations, the flow is locally supercritical downstream of ridges, and transient internal hydraulic jumps result. As the flow relaxes each half tidal period, these jumps are released as internal wave packets, which propagate up into the thermocline. The internal hydraulic jumps are a source of mixing in the valleys, while the small-scale shears associated with the internal waves could lead to mixing higher up the water column. Over the forcing range considered, the response is dominated by slightly higher harmonics of the tidal forcing frequency than predicted by existing analytic theories.

## 1 Introduction

The possibility that the tides act as an important source of energy for diapycnal mixing in the ocean, of similar magnitude to the winds, has been revived by recent measurements of tidal dissipation (Egbert and Ray, 2000) and spatially inhomogeneous diapycnal mixing (Ledwell et al, 2000). Baines (1982) examined the problem of barotropic to baroclinic tidal energy conversion on continental slopes, and concluded that only a small amount of energy would be converted, in part because the dominant tidal flow is parallel to the coast for much of the ocean. Baines however neglected the possibility of topographic variations in the along-slope direction. A region containing such topography in the form of corrugations aligned up and down the slope is the Atlantic continental slope off the South-East United States, where the recent Turbulence and Waves on Irregular Sloping Topography (TWIST) field program was carried out (Nash et al, 2003). In a companion paper (Legg, 2002) we examined the baroclinic response to the barotropic tide component normal to the continental shelf break in a region such as the TWIST site, through a series of numerical simulations. Here we focus on the response to the barotropic tide in the along-slope direction, i.e. parallel to the shelf-break.

Principal features of this region are a concave slope, steepest near the shelfbreak, and less steep further down the slope; a non-uniform stratification, with much stronger stratification near the surface than at depth; and corrugations of small horizontal scale ( $\approx 3\text{km}$ ) aligned up and down the slope. Enhanced mixing was observed over the corrugations.

Previous studies of internal wave generation by flow over topography have identified two important controlling parameters. The first  $\epsilon = |\nabla h|/s$  is a measure of the relative steepness of the topography, where  $h$  is the topographic height, and  $s$  is the slope of an internal wave group velocity

characteristic:

$$s = \left( \frac{\omega^2 - f^2}{N^2 - \omega^2} \right)^{1/2} \quad (1)$$

$\omega$  is the internal wave frequency,  $f$  is the coriolis frequency, and  $N$  is the buoyancy frequency.

The second important parameter,  $R_L = U_0 L / \omega_0$ , where  $L$  is the topographic wavenumber, is a measure of the nonlinearity, expressed as a ratio between the tidal excursion distance  $U_0 / \omega_0$  and the wavelength of the topography  $\lambda = 2\pi / L$ , where  $U_0$  is the amplitude of the barotropic flow forcing, and  $\omega_0$  is the frequency of the forcing. This parameter can also be thought of as a Froude number, being a measure of the ratio of the advection speed to the horizontal phase speed of the fundamental frequency wave  $C_p = \omega_0 / L$ . When  $R_L > 1$ , fundamental frequency waves cannot propagate upstream against the barotropic flow at peak amplitude.

Bell (1975a,b) considered the limit of  $\epsilon \ll 1$ , with finite  $R_L$ . He showed that for small  $R_L$ , the “acoustic limit”, the internal wave response is confined to the forcing frequency, while at large  $R_L$  (e.g. large  $U_0$  or small  $\omega_0$ ), the quasi-steady lee-wave limit applies. For intermediate  $R_L$  the response consists of internal waves at the harmonic frequencies  $n\omega_0$ , up to a maximum frequency of  $N$ . For sinusoidal topography of the form  $h = h_0 \sin(Ly)$ , the vertical velocity amplitude of the generated radiating wave of frequency  $n\omega_0$  is

$$w_n = \frac{n\omega_0}{\pi} h_0 J_n(LU_0 / \omega_0) \quad (2)$$

where  $J_n$  is the Bessel’s function of order  $n$ . and the horizontal wavenumber of the wave is equal to the topographic wavenumber  $L$ . The vertical wavenumber is determined from the dispersion relation for each frequency component. Recent theoretical (Balmforth et al, 2002; St Laurent et al, 2003) and numerical studies (Khatiwala (2003), Li (2003)) have extended Bell’s theory to steeper topography. For  $\epsilon \rightarrow 1$  the internal wave response is characterized by smaller horizontal and vertical scales, as internal wave energy radiates out from the topography in the form of a narrow beam. In addition the numerical simulations of Khatiwala (2003) suggest that for steep sinusoidal topography ( $\epsilon > 1$ ), the effective barotropic to baroclinic energy conversion is reduced, perhaps because the fraction of energy radiated downward into the valleys is dissipated locally.

It should be noted that the theoretical extensions of Balmforth et al (2002) and St Laurent et al (2003) were for the limit  $R_L \ll 1$ , and so there are no theoretical predictions of the modifications expected for large  $R_L$  and large  $\epsilon$ . Baines (1982) also studied the  $R_L \ll 1$  limit.

A second theoretical approach relevant to the TWIST scenario is that of Thorpe (1992, 1996), who considered flow over corrugations in the quasi-steady limit ( $\omega_0 = 0$ ), now on an infinite sloping plane at an angle  $\alpha$  to the horizontal. For corrugations of wavenumber  $L$  aligned up and down the slope, the wavenumber of the internal waves generated by the flow is equal to  $L$  in the alongslope direction, as for the flat-bottomed case. The wavenumber in the direction aligned with the slope is zero (there is no phase difference up and down the slope), and combined with the dispersion relation this gives a vertical wavenumber  $m$  and cross-slope wavenumber  $k$

$$m = - \frac{\cos\beta \cos\alpha L}{\sqrt{(\sin^2\beta - \sin^2\alpha)}} \quad (3)$$

$$k = -\frac{\cos\beta\sin\alpha L}{\sqrt{(\sin^2\beta - \sin^2\alpha)}} \quad (4)$$

(where negative values of  $k$  and  $m$  imply energy propagation toward the shelf-break and upward respectively) where  $\beta = \text{atan}(s)$ , the angle the wave group velocity makes with the horizontal. No wave can be generated for  $\alpha > \beta$ , i.e. for supercritical background slopes such that  $dh/dx > s$ . In the quasi-steady limit, the relevant frequency on which  $s$  depends is the intrinsic frequency of the flow  $U_0L$ , but equations 3 and 4 would be expected to hold equally for waves of frequency  $n\omega_0$  generated by a flow oscillating at frequency  $\omega_0$ .

The TWIST site differs from the scenarios considered in these theoretical studies in several important respects. Firstly, the background slope is not uniform, but changes from a subcritical slope ( $\alpha < \beta$ ) with respect to the M2 tidal frequency on the lower reaches, to a supercritical slope on the upper part of the slope. Secondly, the amplitude of corrugations, while small, may in places be sufficient to give locally steep slopes in the direction parallel to the shelf-break, so that  $\epsilon > 1$  in the direction of the flow. Thirdly, the forcing amplitude might be sufficiently large that  $R_L > 1$ . In this study we focus on the modifications to the baroclinic flow generated by tidal flow over sloping corrugated topography when the background slope is concave, and corrugations and forcing are of finite amplitude.

## 2 Model formulation and configuration

As described in Legg 2002, we use the nonhydrostatic MIT ocean model (Marshall et al, 1997), with the coordinate system oriented with the continental slope: the x-direction is the cross-slope direction, and the y-direction is the along-slope direction. The domain size is  $L_x \times L_y \times H = 254\text{km} \times 10\text{km} \times 2505\text{m}$ , and the resolution is  $nx \times ny \times nz = 328 \times 80 \times 60$ , and variable grids are employed in the x and z directions, with minimum values of  $\Delta z = 10\text{m}$  and  $\Delta x = 370\text{m}$ , located in the thermocline and over the slope respectively. The topography consists of the along-slope average of the observed topographic height, with sinusoidal corrugations, of wavelength  $\lambda = 10/3\text{km}$ , and amplitude  $h_0$  superimposed. The density field is initially horizontally uniform, with a vertical stratification which is a power law best-fit to the observed density field. The vertical and horizontal viscosities are  $A_v = 3 \times 10^{-2}\text{m}^2/\text{s}$  and  $A_h = 1\text{m}^2/\text{s}$  respectively, the minimum values found to prevent grid-scale noise, given the relatively coarse grids. The explicit background diffusivity is set to zero, to avoid erosion of the background thermocline stratification in the absence of flow. Implicit numerical diffusion is introduced where needed for stability by the tracer advection scheme - a direct discretization method with flux limiting (Pietrzak, 1998).

At the topography, no-slip boundary conditions are imposed. A linear free-surface boundary condition is applied at the ocean surface. At the coast and the offshore boundary stress-free boundary conditions are imposed, while at the  $y = 0, L_y$  cross-slope boundaries, periodic boundary conditions are applied. The tidal forcing is applied through a body force of the form

$$\frac{\partial v}{\partial t} = U_0\omega_0\cos(\omega_0 t) \quad (5)$$

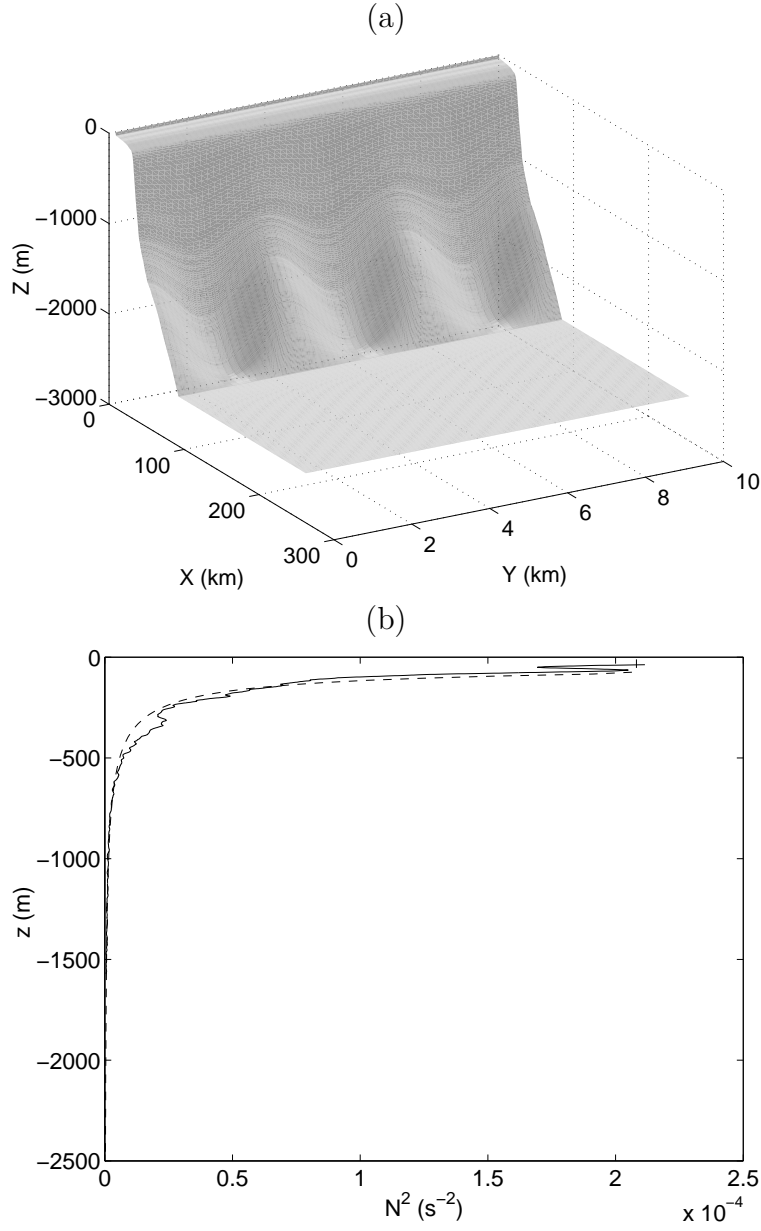


Figure 1: (a) The topography used in the model. The mean slope is an alongslope average of the actual topography of the Twist region. Sinusoidal along-slope variations are superimposed on this mean slope, with a wavelength of  $10/3$  km. (b) The stratification  $N^2 = -(g/\rho_0)d\rho/dz$ , as a function of depth, from the observations (solid line) and a monotonic bestfit powerlaw profile of the form  $N^2 = 1.1007(-z)^{-1.9564}$  for  $z < -80$  m, and  $N^2 = 1.1007 \times 80^{-1.9564}$  for  $z > -80$  m.

Simulation	$U_0$	$h_0$	$R_L = U_0 L / \omega_0$	$\epsilon_y = 2\pi h_0 / (\lambda s)$	topography	stratification
<i>U2h100</i>	2 cm/s	100m	0.27	1.2	concave	nonuniform
<i>U2h300</i>	2 cm/s	300m	0.27	3.7	concave	nonuniform
<i>U10h100</i>	10 cm/s	100m	1.34	1.2	concave	nonuniform
<i>U10h300</i>	10 cm/s	300m	1.34	3.7	concave	nonuniform
<i>UniformN</i>	2 cm/s	100m	0.27	2.9	concave	uniform
<i>UniformS</i>	2 cm/s	100m	0.27	2.9	linear	uniform

Table 1: Parameters for different runs.

where  $v$  is the along-slope velocity. The boundary conditions at the coast and offshore boundary have little influence on the solutions, since the waves generated on the slope do not reach either boundary during the time of integration. The forcing frequency  $\omega_0$  is set to the M2 tidal frequency of  $\omega_0 = 1.41 \times 10^{-4} s^{-1}$ . No-flux boundary conditions are applied to the active tracer, and a linear equation of state is employed.

We describe a series of different runs characterized by different forcing amplitude  $U_0$  and different corrugation amplitude  $h_0$ , listed in Table 1. These two parameters can equivalently be described by the nondimensional parameters  $R_L = U_0 L / \omega_0$ , a measure of nonlinearity and  $\epsilon_y = 2\pi h_0 / (\lambda s)$ , a measure of the maximum corrugation steepness relative to the wave steepness (where we use  $s$  appropriate to the fundamental frequency  $\omega_0$ ). Most of the calculations have the concave slope and nonlinear stratification of the observation region. In addition, to evaluate the role of the concave slope and nonuniform stratification, we include two other calculations, one with uniform stratification and concave slope, the other with uniform stratification and uniform slope. This latter calculation, henceforth identified as *UniformS*, comes closest to the conditions in the theoretical model of Thorpe (1992). Note that all calculations have  $\epsilon_y > 1$ , so that the corrugations are locally steep, and  $R_L > 1$  for the calculations with  $U_0 = 0.1$ , so that the peak barotropic current speed is greater than the horizontal phase speed of the fundamental frequency wave.

## 3 Results

### 3.1 Reference calculation

We first describe in detail our “reference calculation”, which has concave slope, nonuniform stratification and forcing amplitude  $U_0 = 2 \text{ cm/s}$  and corrugation amplitude  $h_0 = 100 \text{ m}$ . Henceforth we will refer to this calculation as *U2h100*.

Snapshots of the vertical velocity field at a time  $t = 3.23T$  (where  $T$  is the M2 tidal period) after the onset of the calculation reveal the character of the wave field. The lengthscale in the alongslope direction is equal to that of the corrugations. In the cross-slope direction, velocities are in phase in a direction roughly aligned with the slope, all in agreement with predictions of linear theory (Thorpe, 1992).

Figure 3 shows, for a wave generated over the corrugations at a depth of  $h = 2370 \text{ m}$ , the

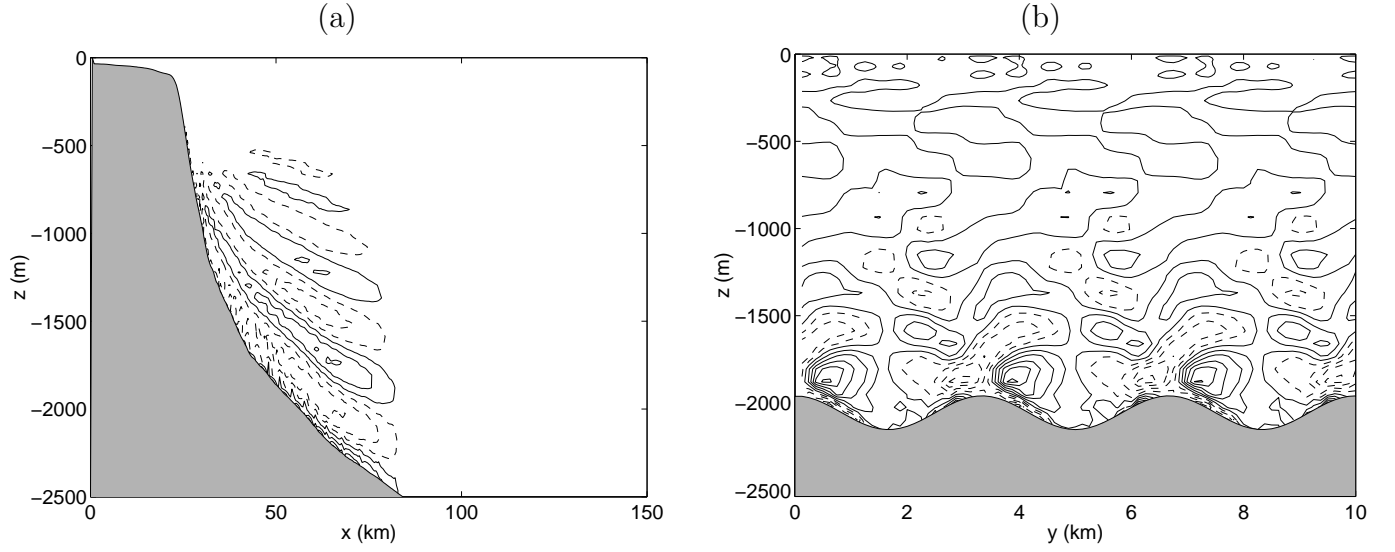


Figure 2: Instantaneous vertical velocity fields at a time  $t = 3.23T$  for the reference calculation  $U2h100$  with  $U_0 = 2\text{cm/s}$  and  $h_0 = 100\text{m}$  (a) in the  $(x,z)$  plane at a location on the flanks of a ridge ( $y=2.5\text{km}$ ) (b) in the  $(y,z)$  plane at  $x=58.7\text{km}$ . Contour spacing =  $5 \times 10^{-4}\text{m/s}$ . In this and all subsequent plots, dashed contours represent negative values (i.e. downward vertical velocities).

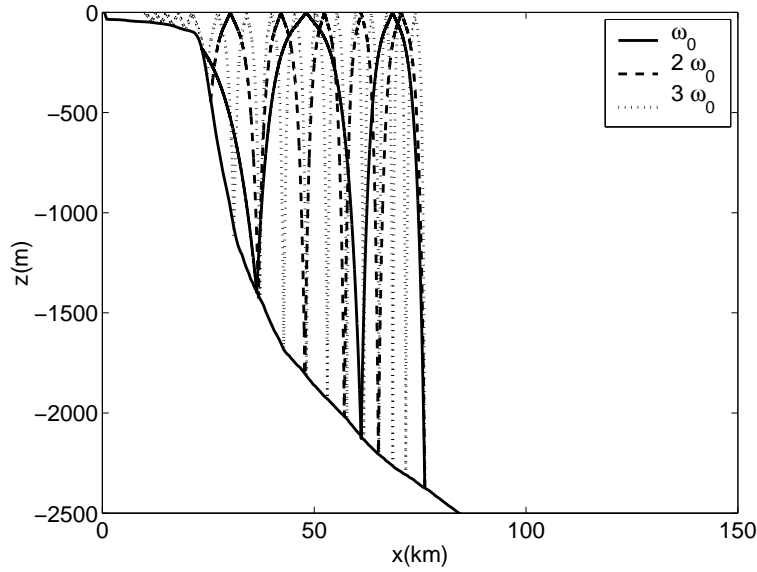


Figure 3: The projection of the internal wave characteristics onto the  $(x,z)$  plane, for internal waves at frequencies  $\omega_0$ ,  $2\omega_0$  and  $3\omega_0$ , generated at location of depth  $h = 2370\text{m}$  on a concave slope, by alongslope flow over corrugations of wavelength  $\lambda = 10/3\text{km}$ , for nonuniform stratification as in figure 1b.

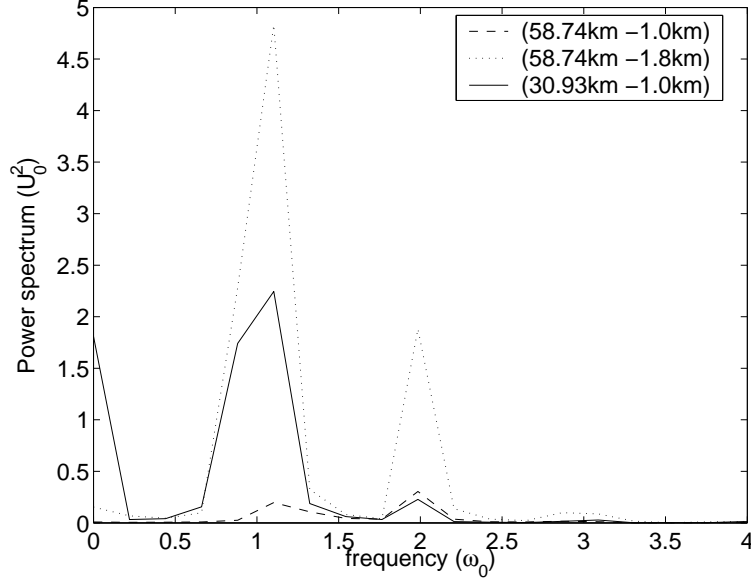


Figure 4: The power spectrum of the vertical velocity  $P = \hat{w}(\omega)\hat{w}^*(\omega)$ , where  $\hat{w}(\omega) = \int_{-\infty}^{\infty} w(t)\exp(i\omega t)dt$ , the Fourier transform of the vertical velocity timeseries. The power spectrum is given for 3 different locations:  $(x, z) = (58.74km, -1.0km), (58.74km, -1.8km), (30.93km, -1.0km)$ , where the first (dashed) is far from the slope, and the second (dotted) and third (solid) are just above shallow and steep slope respectively. The spectra are averaged over all points in the alongslope (y) direction.

projection of the wave characteristics onto the (x,z) plane, for waves of frequency  $\omega_0$ ,  $2\omega_0$  and  $3\omega_0$ . The initial wavenumbers are given from equations 3 and 4, assuming the local stratification and slope appropriate to that depth. (The variation of the background slope on the concave slope is ignored in estimating these wavenumbers). At each reflection from the top surface, the horizontal wave numbers are unchanged in magnitude and direction, while the vertical wavenumber changes sign. Subsequent reflections from the slope tend to increase the magnitude of the wavenumbers in the vertical and cross-slope direction, while the wavenumber in the along isobath direction remains constant (Thorpe, 1996). With variable stratification, the vertical wavenumber is increased as stratification increases, so that the slope of the characteristic  $k/m$  flattens. All waves propagate toward shallower water initially (Thorpe, 1996), but the waves at frequencies  $\omega_0$  and  $2\omega_0$  encounter supercritical slope and are reflected offshore, while the  $3\omega_0$  wave continues onshore. Note that higher frequencies lead to many more reflections in traveling a fixed horizontal distance toward the shelfbreak.

Vertical velocity power spectra are shown in figure 4 for three different locations. Close to the topography ((58.74km,-1.8km) and (30.93km,-1.0km)), the largest spectral peak is at a frequency of  $\omega_0$ , even for the steep slope (30.93km, -1.0km) where disturbances at this frequency are evanescent. However, away from the topography (e.g. at  $(x, z) = (58.74km, -1.0km)$ ) the peak at  $2\omega_0$  is greatest.



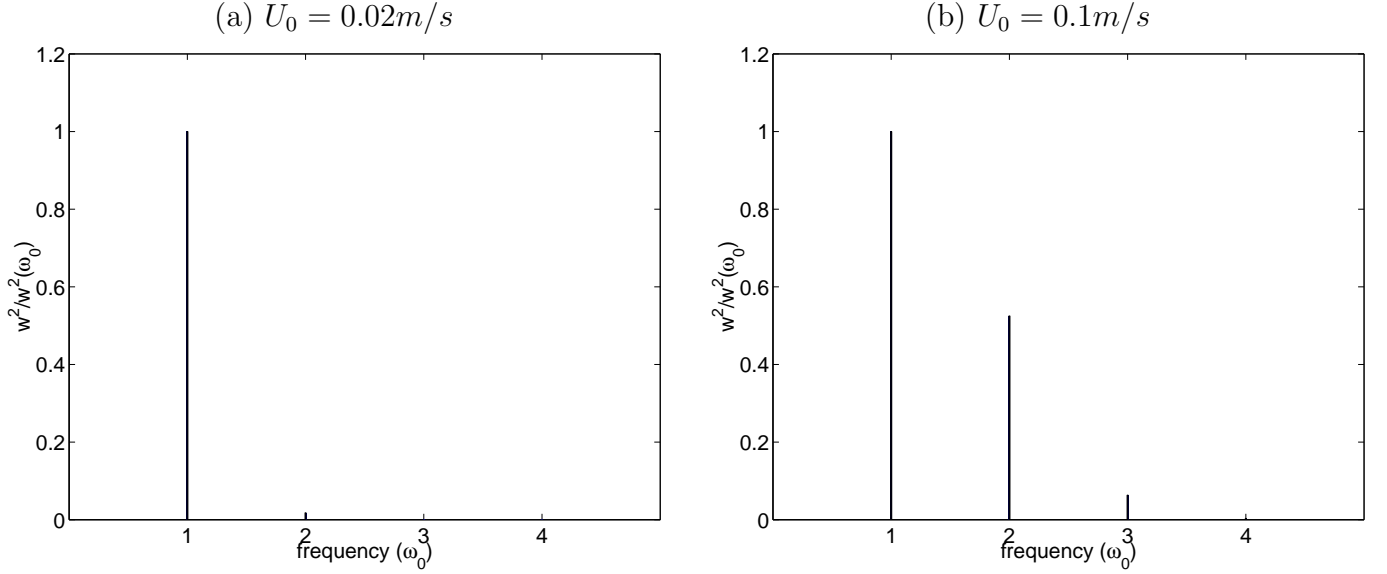


Figure 5: Vertical velocity power spectrum predicted from equation 2, normalized by  $w^2(\omega_0)$  for (a)  $U_0 = 2\text{cm/s}$  and (b)  $U_0 = 10\text{cm/s}$ .

For comparison, the spectral shape predicted by Bell (from eqn 2) is shown in figure 5. For a forcing velocity of  $U_0 = 2\text{cm/s}$ , Bell predicts the largest spectral peak at  $\omega_0$ . Note however this prediction is made for a zero background slope.

The vertical velocity is plotted as a function of time and distance in figure 6. Overlain on these plots are lines of constant phase calculated from the phase velocity  $\mathbf{C_p} = (C_x, C_y, C_z)$  where

$$(C_x, C_y, C_z) = \left( \frac{\omega}{k}, \frac{\omega}{l} - U, \frac{\omega}{m} \right) \quad (6)$$

and  $\mathbf{K} = (k, l, m)$  is the wavenumber. From Thorpe (1992) we use  $l = L$ , where  $L$  is the topographic wavenumber.  $k$  is determined from equation 4 where  $\alpha$  is the local slope angle, and the stratification at the slope is used.  $l$  and  $k$  do not change with depth, but  $m$ , the vertical wavenumber does change due to the change in stratification according to

$$\frac{(k^2 + l^2)^{1/2}}{m} = \left( \frac{\omega^2 - f^2}{N^2 - \omega^2} \right)^{1/2} \quad (7)$$

so that

$$C_z = \frac{\omega}{(k^2 + L^2)^{1/2}} \left( \frac{\omega^2 - f^2}{N^2 - \omega^2} \right)^{1/2} \quad (8)$$

For each plot we use values of  $\omega = \omega_0, 2\omega_0, 3\omega_0$ , except at locations where the slope is supercritical with respect to the fundamental frequency, when only the higher frequencies are shown. In estimating the along-slope phase speed in a stationary frame of reference,  $C_y$ , (figure 6b) the flow speed

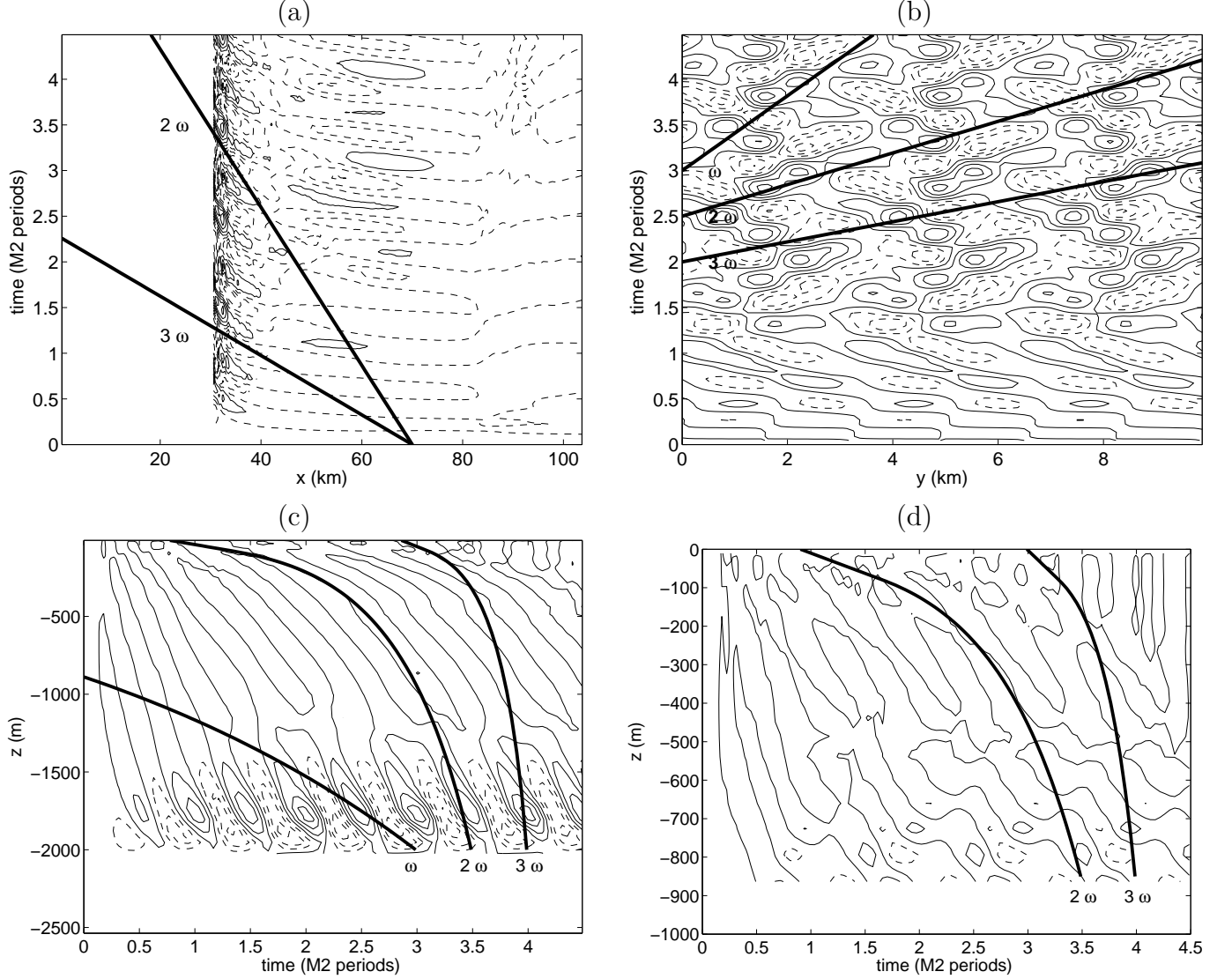


Figure 6: Vertical velocity in *U2h100* as a function of time and (a)  $x$ , at  $y = 3.37\text{km}$ , and  $z = -1.00\text{km}$ , (b)  $y$ , at  $x = 58.7\text{km}$  and  $z = -1.00\text{km}$  (c)  $z$ , at  $x = 58.7\text{km}$  and  $y = 3.37\text{km}$  and (d)  $z$  at  $x = 29.08\text{km}$  and  $y = 3.37\text{km}$ . Contour spacings are (a)  $2.5 \times 10^{-4}\text{m/s}$ , (b)  $2 \times 10^{-4}\text{m/s}$ , (c)  $5 \times 10^{-4}\text{m/s}$ , (d)  $5 \times 10^{-4}\text{m/s}$ . Overlain on the plots are the lines of constant phase for frequencies  $\omega_0$ ,  $2\omega_0$  and  $3\omega_0$ . In (a) and (d) only the two higher harmonic frequencies are shown since the slope is supercritical to the fundamental at this location. The higher the frequency, the faster the phase velocity.

$U$  must be removed. For convenience we use  $U = U_0$ , the peak barotropic flow velocity (giving a lower limit of the actual phase speed in the stationary frame) although in actual fact the flow is oscillating.

In figure 6a vertical velocity is shown as a function of  $x$  and time, on a plane located at a depth of  $z = -1.0km$ , and  $y = 3.37km$  (situated over a ridge). No values are shown for  $x < 30.6km$  since this plane intersects the topography at this location. The lines of constant phase have been calculated using the value of slope and stratification where the plane intersects the topography. At this location, the slope is supercritical with respect to the fundamental frequency  $\omega_0$ , but not with respect to  $2\omega_0$  and  $3\omega_0$ , for which the theoretical constant phase lines are drawn. We see that close to the topography, the velocity field does appear to correlate with the  $2\omega_0$  theoretical constant phase line appropriate to this slope. Phase propagation is toward the slope, as predicted by Thorpe (1992). Further away from the slope, the numerical results indicate faster phase velocities, which are expected if the waves here were generated over less steep slope (hence smaller  $k$ ).

In figure 6b the vertical velocity is shown as a function of  $y$  and time, again at  $z = -1.0$  and now at  $x = 58.7km$ . Since  $C_y$  depends only on the frequency and the wavenumber of the topography, and the background flow speed, no choices about stratification or slope have to be made in this case in plotting the theoretical lines of constant phase. The broader features of the numerical velocity pattern appear to follow the  $2\omega_0$  constant phase line most closely. Here phase propagation occurs alternately in each direction, corresponding to waves with wavenumber  $\pm L$ , as expected from an oscillating forcing flow. For this value of  $R_L = 0.26$ , the background flow has only a small influence on the lines of constant phase.

The two final panels of figure 6 show the vertical velocity as a function of  $z$  and time, for two locations on the ridge at  $y = 3.37km$ , with  $x = 58.7km$  and  $x = 29.08km$  respectively. At the second location, the slope is supercritical with respect to the fundamental frequency so the theoretical lines of constant phase are shown only for  $\omega = 2\omega_0, 3\omega_0$ . The lines of constant phase are calculated from equation 8 for waves generated at the slope at this location, with the stratification given at the slope. At both locations the numerical velocity patterns are aligned closely with the lines of constant phase with frequency  $2\omega_0$ . Phase propagation is downward, indicating upward energy propagation, as expected for waves generated at the bottom boundary.

Since the theoretical lines of constant phase align closely with the patterns of vertical velocity close to the slopes, we therefore see that close to the concave topography, the vertical and horizontal wavelengths are given by the values predicted for waves generated locally at the slope. Further away from the slope (e.g. for large  $x$  in figure 6a) the source of the wave is less clear, but the horizontal wavelength  $\lambda_x$  increases as the bottom slope reduces, as expected.

An interesting feature is the generation of waves at the higher harmonic frequencies in locations where the slope is supercritical to the fundamental frequency. (It should be noted that the slope is also supercritical to the maximum intrinsic frequency of the flow  $U_0 L$ .) Hence tides can still generate a wave response when flowing over steep slopes, if higher harmonics are included. From figure 6a it can be seen that right at the steep slope the vertical velocity signal has frequency equal to  $\omega_0$ , but presumably since  $\omega_0$  waves cannot propagate away from the slope, a short distance away from the slope the signal has the higher frequency  $2\omega_0$ .

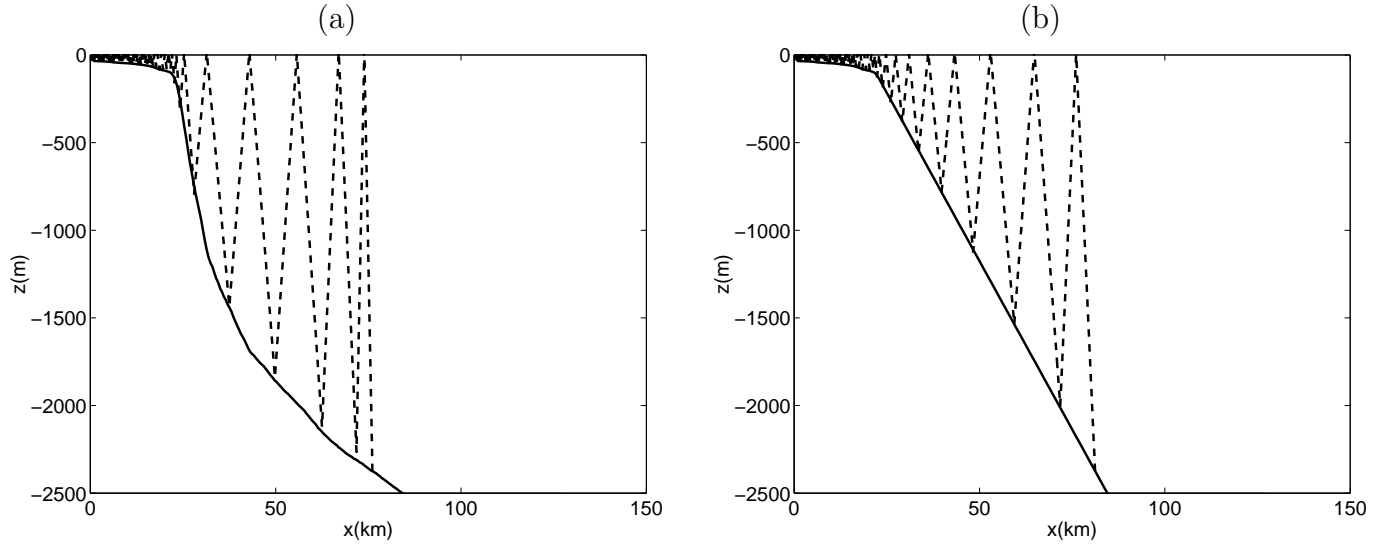


Figure 7: The projection of the internal wave characteristics onto the  $(x,z)$  plane, for an internal wave at frequency  $2\omega_0$ , (where  $\omega_0$  is the M2 tidal frequency) generated at a location of depth  $h = 2370m$ , by alongslope flow over corrugations of wavelength  $\lambda = 10/3km$ . (a) uniform stratification, concave slope *UniformN*, (b) uniform stratification, linear slope *UniformS*.

### 3.2 Influence of concave slope and nonuniform stratification

We now compare the results from the reference calculation *U2h100* with two calculations with the same amplitude topography and barotropic forcing; the first *UniformN* has the same concave slope as *U2h100* but the nonuniform stratification is replaced with stratification with a constant value of  $N = 6.19 \times 10^{-4}s^{-1}$ ; the second *UniformS* also has uniform stratification and in addition the concave slope is replaced with a uniform slope between the shelfbreak and the base of the slope.

Figure 7 shows the projection of the  $2\omega_0$  wave onto the  $(x,z)$  plane, for a wave generated at a depth of 2370m, for *UniformN* and *UniformS*. This particular frequency is chosen since it seems to dominate the spectra far from the bottom topography (figure 2). The choice of constant stratification value has been made so that the wave undergoes a similar number of reflection from the slope as it moves toward the shelf as in the case with variable stratification. The concave slope is supercritical to this frequency over a small region near the top (although this particular characteristic does not encounter that portion of slope, and hence wave energy can reach the shelf) while the uniform slope is subcritical throughout.

Figures 8 and 9 show snapshots of the vertical velocity for *UniformN* and *UniformS* respectively. Compared to figure 2 the most significant feature is that the fields become quite disorganized with time. At earlier times, the velocity patterns in figures 8a and 9a are aligned with the background slope, as expected, but at later times there is little organized pattern. Similar behavior is seen in the  $(y,z)$  plane cross-sections. Changing the stratification from a variable profile to a constant value has much more impact on the character of the flow than changing the slope from concave to

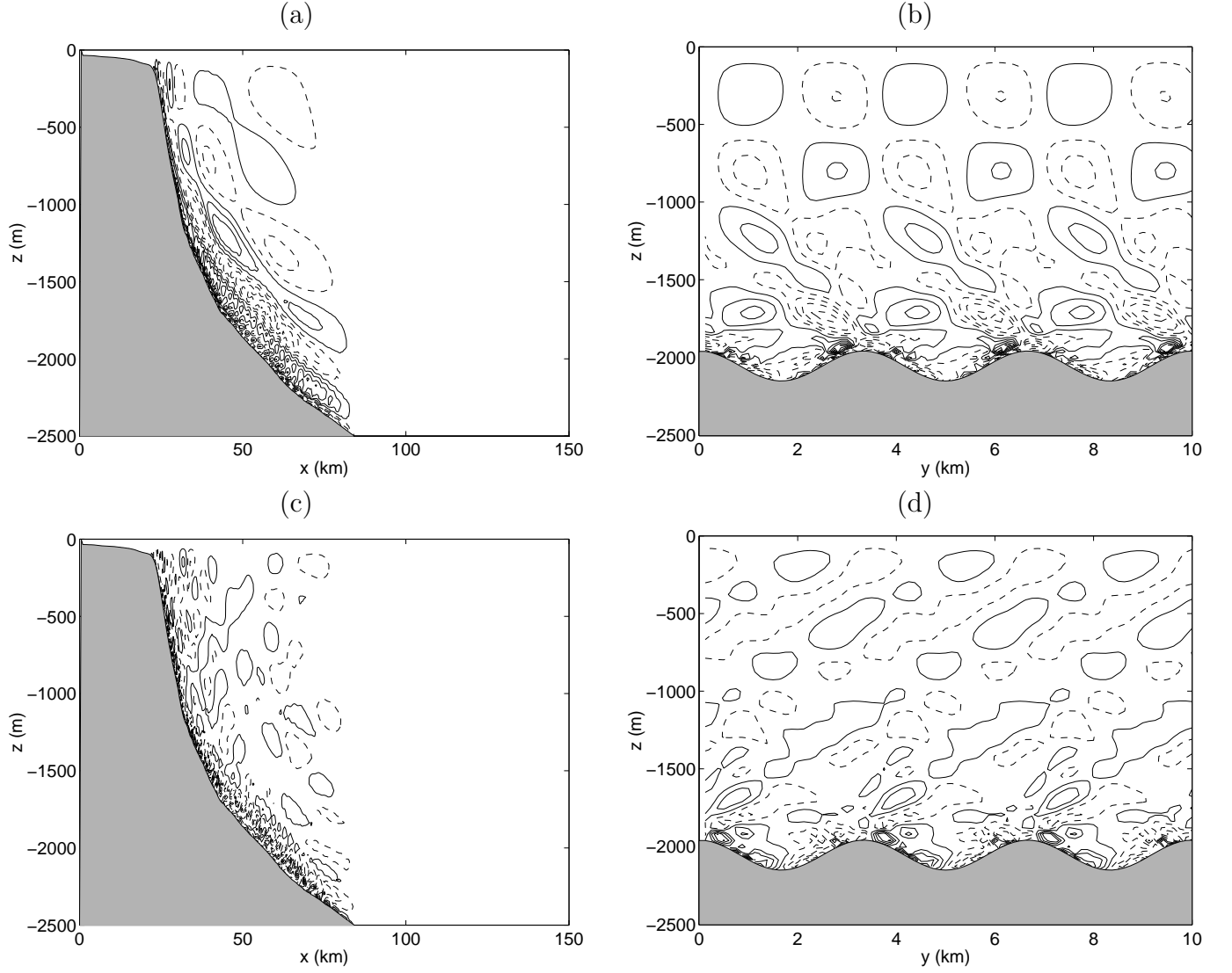


Figure 8: Instantaneous vertical velocity fields for the calculation with uniform stratification  $N = 6.2 \times 10^{-4}$  and concave slope, *UniformN*. (a) at  $t = 0.67T$  in the  $(x,z)$  plane at a location on the flanks of a ridge ( $y=2.5\text{km}$ ) (b) at  $t = 0.67T$  in the  $(y,z)$  plane at  $x=58.7\text{km}$ . (c) at  $t = 3.23T$  in the  $(x,z)$  plane at a location on the flanks of a ridge ( $y=2.5\text{km}$ ) (d) at  $t = 3.23T$  in the  $(y,z)$  plane at  $x=58.7\text{km}$ . Contour spacing =  $2 \times 10^{-4} \text{m/s}$

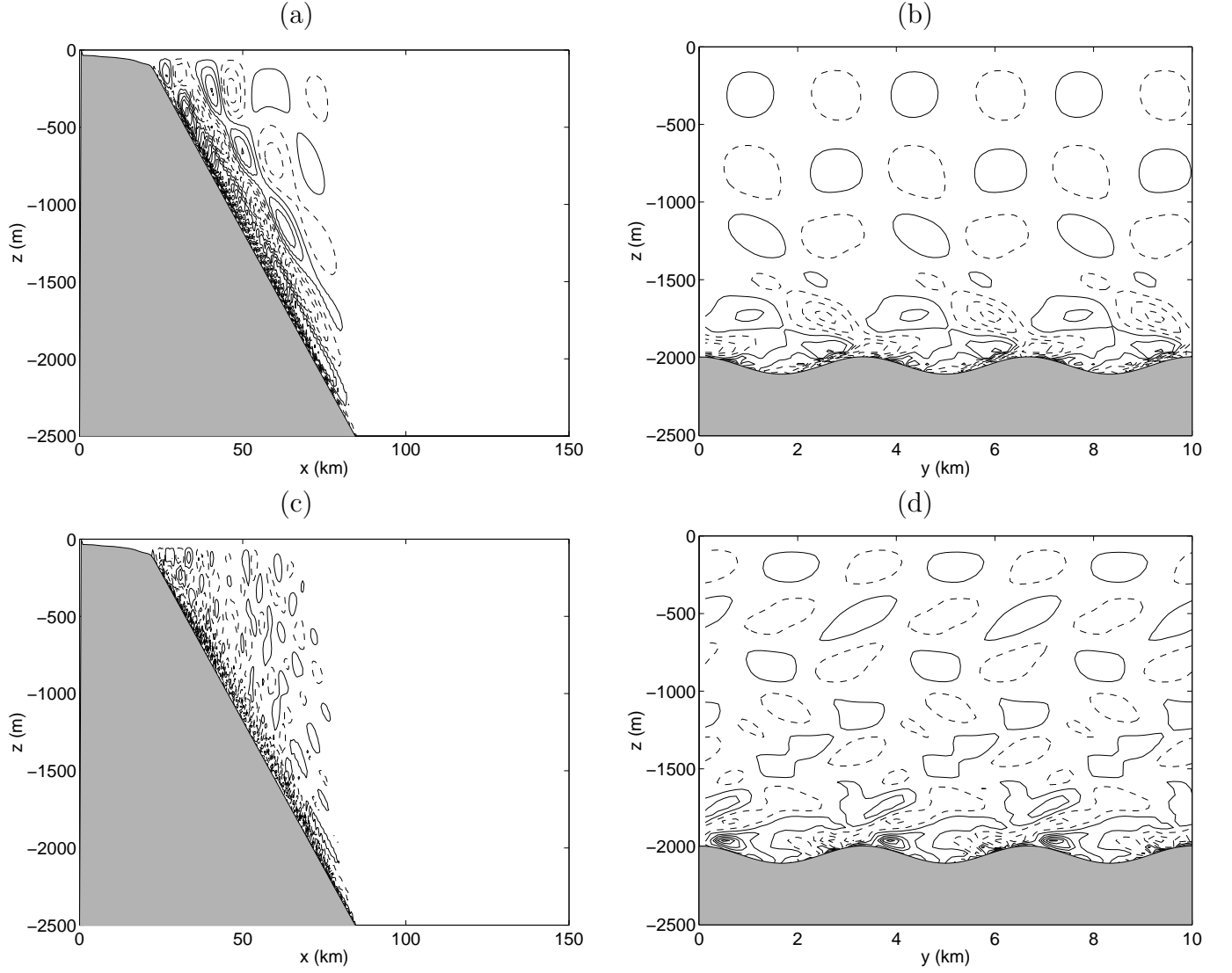


Figure 9: Instantaneous vertical velocity fields for the calculation with uniform stratification  $N = 6.2 \times 10^{-4}$  and uniform slope, *UniformS*. (a) at  $t = 0.67T$  in the  $(x, z)$  plane at a location on the flanks of a ridge ( $y=2.5\text{km}$ ) (b) at  $t = 0.67T$  in the  $(y, z)$  plane at  $x=58.7\text{km}$ . (c) at  $t = 3.23T$  in the  $(x, z)$  plane at a location on the flanks of a ridge ( $y=2.5\text{km}$ ) (d) at  $t = 3.23T$  in the  $(y, z)$  plane at  $x=58.7\text{km}$ . Contour spacing  $= 2 \times 10^{-4} \text{m/s}$

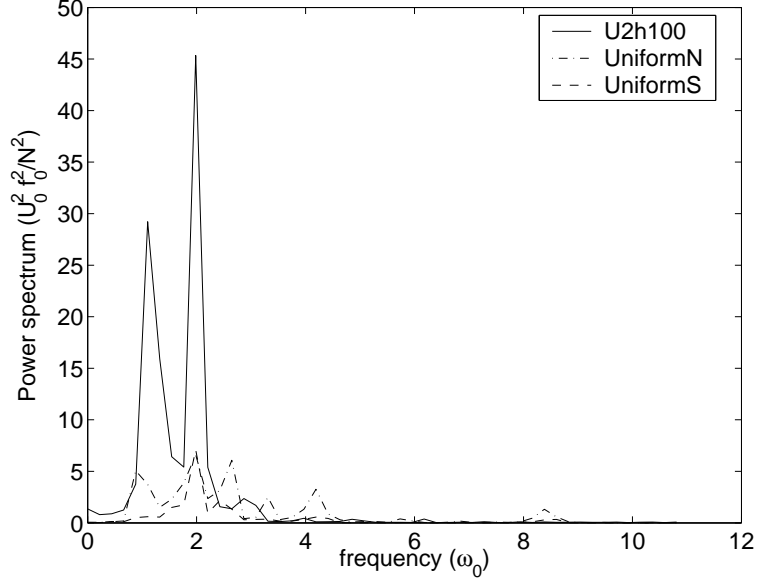


Figure 10: The power spectrum of the vertical velocity  $P = \hat{w}(\omega)\hat{w}^*(\omega)$ , where  $\hat{w}(\omega) = \int_{-\infty}^{\infty} w(t)\exp(i\omega t)dt$ , the Fourier transform of the vertical velocity timeseries. The power spectrum is given for 3 different calculations: *U2h100* (solid), *UniformN* (dot-dash) and *UniformS* (dashed), at a location  $(x, z) = (58.74\text{km}, -1.0\text{km})$ , for the two cases with concave slope and  $(x, z) = (72.83\text{km}, -1.0\text{km})$  for the case with uniform slope. In all three, the total water depth at this location (averaged in the alongslope direction) is  $2\text{km}$ , so that the spectrum is taken far above the slope. The spectra are averaged over all points in the alongslope ( $y$ ) direction.

uniform.

Figure 10 shows the vertical velocity power spectra at a height  $1\text{km}$  above the slope, where the total depth is  $2\text{km}$ , for all three calculations *U2h100*, *UniformN*, *UniformS*. The spectra are divided through by  $N(z)^2/f_0^2$ , to facilitate comparison between the calculations of different stratification, where vertical velocity in internal waves is expected to be smaller as stratification is increased, due to the greater energy required to deform the isopycnals. Even with this scaling, the vertical velocity magnitudes in the calculations with constant stratification are smaller than the uniform stratification case. The principal peaks are again at  $2\omega_0$ , but there is relatively more energy at higher harmonics. Note that  $N/\omega_0 = 10.7$  for the constant stratification, while for the nonuniform stratification, the maximum possible frequency generated on the slope at  $x = 58.7\text{km}$  is  $4\omega_0$ , given the stratification at the height of the topography.

We now examine the time-distance plots of vertical velocity for *UniformS*, shown in figure 11. Those for *UniformN* are similar in most respects to those of *UniformS* and are therefore not shown. In figure 11c and near the slope in 11d, the vertical velocity patterns are closely aligned with lines of constant phase for frequency of  $2\omega_0$ , but in figure 11a  $\omega_0$  constant phase lines match the slope of velocity patterns better. Note that compared to figure 6a, the numerically calculated vertical velocity patterns in figure 11a do not curve as the slope is approached - this is a result of the

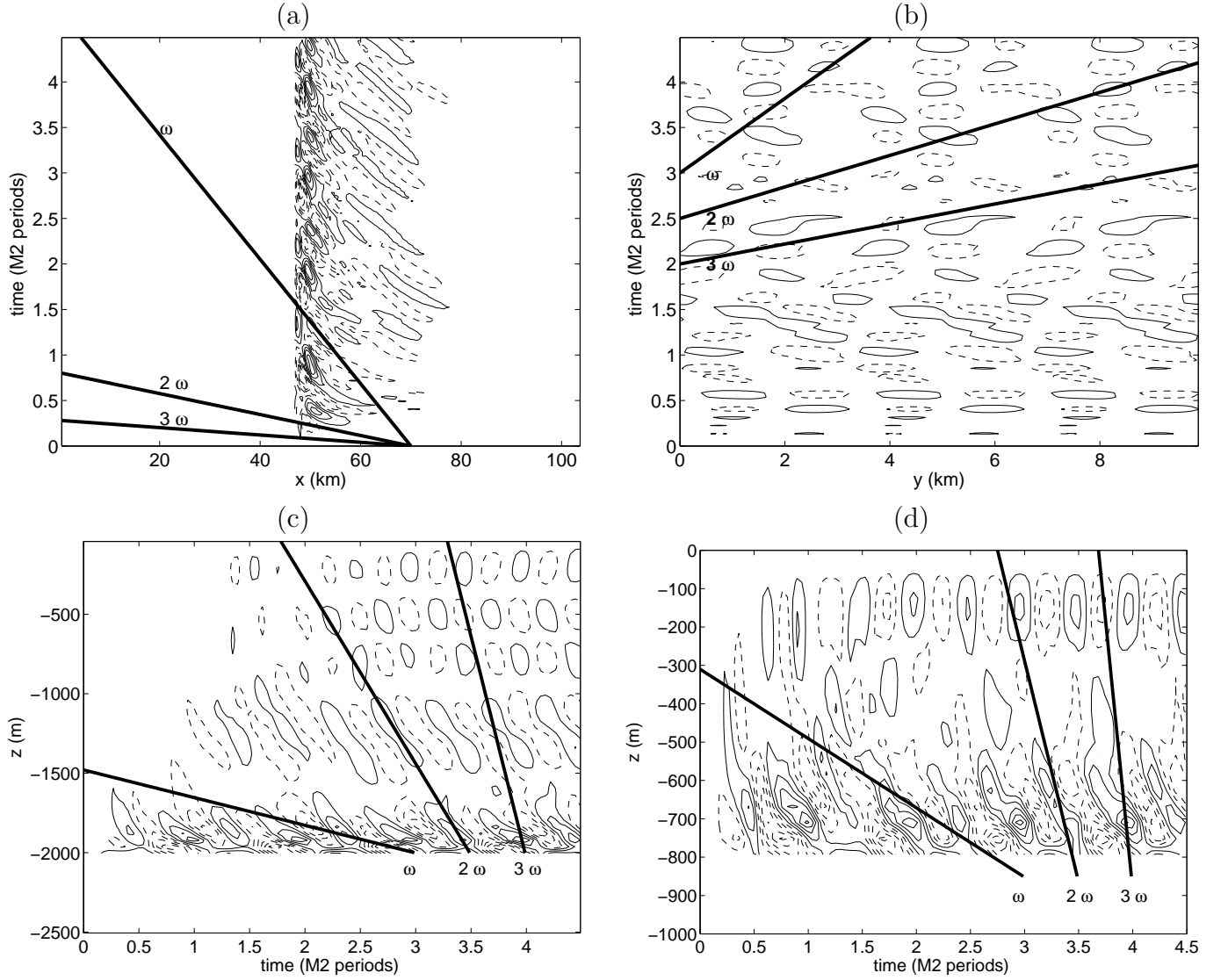


Figure 11: As for figure 6 but for *UniformS*. (a) at  $y = 3.37\text{km}$ , and  $z = -1.00\text{km}$ , (b) at  $x = 72.8\text{km}$  and  $z = -1.00\text{km}$  (c) at  $x = 72.8\text{km}$  and  $y = 3.37\text{km}$  and (d) at  $x = 41.7\text{km}$  and  $y = 3.37\text{km}$ . The locations in  $x$  have been chosen so that the waterdepth is the same as in the plots in figure 6. Contour spacing is  $2 \times 10^{-4}\text{m/s}$ . Lines of constant phase for the waves of frequency  $\omega_0$ ,  $2\omega_0$  and  $3\omega_0$  are superimposed, with higher frequencies having faster phase velocities.



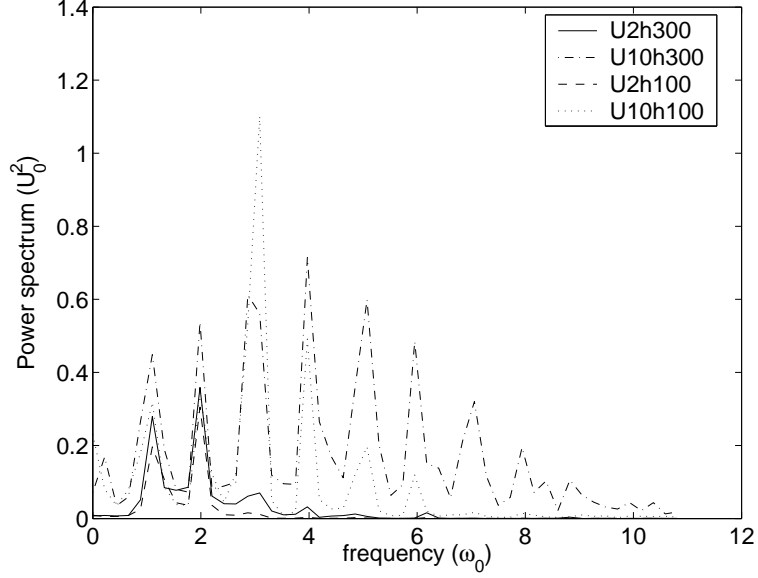


Figure 12: The power spectra of the vertical velocity  $P = \hat{w}(\omega)\hat{w}^*(\omega)$ , for 4 different combinations of  $U_0$  and  $h_0$ , at the location  $(x, z) = (58.74\text{km}, -1.0\text{km})$ , far from the slope, and averaged over all points in the alongslope (y) direction.

constant slope (in *UniformN* these patterns do curve toward the wall, indicating the slower phase speeds of waves generated on steeper slopes). At higher levels in figure 11c and figure 11d and in figure 11b there does not appear to be phase propagation, but rather standing mode behavior in both the along-slope (y) and vertical (z) directions. This is established once the waves reflect from the upper surface. Reflections from the upper surface occur much sooner in the uniformly stratified cases than for the nonuniform stratification due to the faster group velocity in the near surface layers when the thermocline enhancement of stratification is absent.

### 3.3 Influence of flow amplitude and corrugation height

We now examine how increasing the flow amplitude (thereby increasing  $R_L$ ) and increasing the corrugation amplitude (thereby increasing the relative steepness  $\epsilon_y$ ) influence the qualitative features of the flow field. The 4 different calculations are the reference case already described, with  $U_0 = 2\text{cm/s}$ ,  $h_0 = 100\text{m}$  (*U2h100*); *U2h300*, with  $U_0 = 2\text{cm/s}$ ,  $h_0 = 300\text{m}$ ; *U10h100*, with  $U_0 = 10\text{cm/s}$ ,  $h_0 = 100\text{m}$ ; and *U10h300* with  $U_0 = 10\text{cm/s}$ ,  $h_0 = 300\text{m}$ .

The vertical velocity power spectra from all 4 calculations at a location far above the slope are shown in figure 12. At this location the reference calculation has spectral peaks at frequencies of  $\omega_0$  and  $2\omega_0$ . Increasing the topographic amplitude changes the spectrum little. This contrasts with the theoretical predictions from Bell (1975a) (equation 2), which would suggest that the spectral amplitude increases like  $h_0^2$ . More significant changes appear when the flow amplitude is increased: *U10h100* has the largest peak at  $3\omega_0$ , with significant peaks up to  $6\omega_0$ . Increasing the topography amplitude at this high flow-speed increases the amount of energy in higher harmonics, and the

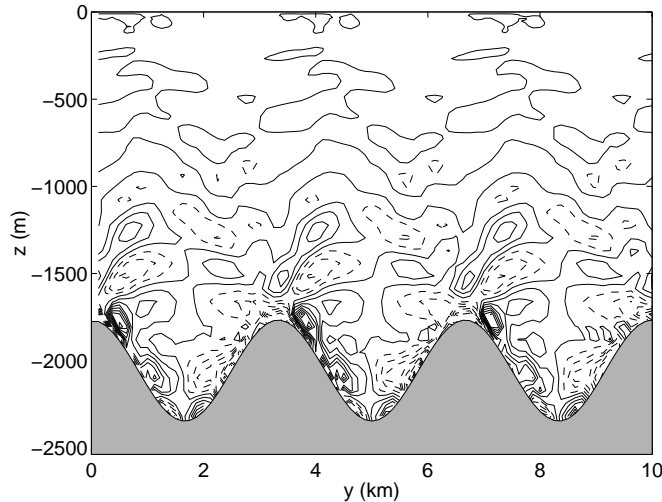


Figure 13: Instantaneous vertical velocity fields at a time  $t = 3.2T$  for  $U2h300$   $U_0 = 2\text{cm/s}$  and  $h_0 = 300\text{m}$  in the  $(y, z)$  plane at  $x=58.7\text{km}$ . Contour spacing =  $5 \times 10^{-4}\text{m/s}$

largest spectral peak for  $U10h300$  is at  $4\omega_0$  (although that at  $3\omega_0$  is only slightly smaller). The amplitudes of the spectra have all been scaled by  $U_0^2$ . The theoretical spectrum predicted from Bell (1975a) (eqn 2) is shown in figure 5b for  $U_0 = 10\text{cm/s}$ . Even at this flow speed, Bell predicts most of the energy will be contained at frequency  $\omega_0$ , with smaller contributions from  $2\omega_0$  and  $3\omega_0$ . In fact Bell predicts a spectral peak at  $3\omega_0$  only for  $U_0 > 24\text{cm/s}$ .

A snapshot of the vertical velocity field in the  $(y, z)$  plane for  $U2h300$  at the same time and location as in figure 2b is shown in figure 13. The amplitude of topography has been increased from  $h_0 = 100\text{m}$  to  $h_0 = 300\text{m}$  (while keeping  $U_0$  fixed). The principal qualitative difference is a tendency for disturbances to be narrower near the top of the ridge (as noted in previous calculations with steep topography, e.g. Khatiwala (2003) and predicted by Balmforth et al (2002)).

The analogous snapshot for  $U10h100$ , an increase in  $U_0$  from  $2\text{cm/s}$  to  $10\text{cm/s}$  while holding  $h_0$  fixed at  $100\text{m}$ , is shown in figure 14. The pattern is again broader, as in figure 2 but now tilted over, as a consequence of the different slope of the characteristics for higher frequencies.

The snapshots in the  $(x, z)$  plane show qualitatively similar features as in figure 2a, and hence are not shown.

When both  $U_0$  and  $h_0$  are increased, as in  $U10h300$ , qualitatively new features appear near the ridges, as seen in figure 15a. This snapshot is taken when the barotropic velocity is at its peak. Large downwelling is seen over the ridges, with similarly large rebound upwelling just downstream. We see that this is associated with a plunging down of isopycnals (figure 15c), followed by a rebound which looks qualitatively like an internal hydraulic jump. The horizontal velocity field (with the barotropic forcing of  $10\text{cm/s}$  subtracted) shows that the flow is accelerated in a thin layer over the ridge, and then reverses direction in the hydraulic jump.

The horizontal velocity field also shows that although the vertical velocity amplitude becomes small as the waves propagate up into the more strongly stratified upper region, the horizontal velocity still contains significant energy. The strongest shears are therefore found in the thermocline.

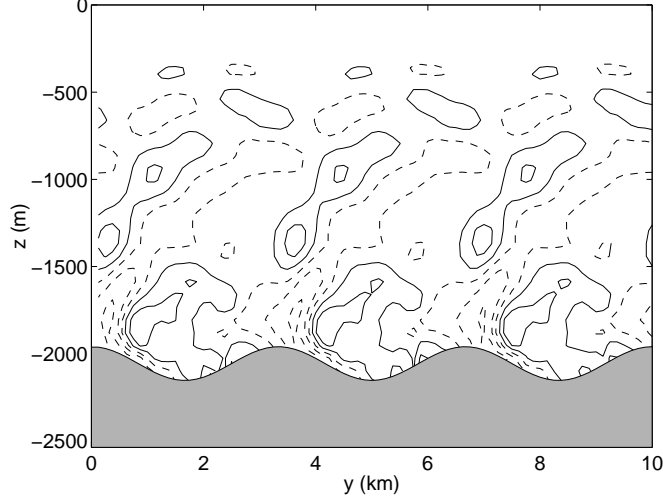


Figure 14: Instantaneous vertical velocity fields at a time  $t = 3.2T$  for  $U10h300$ ,  $U_0 = 10\text{cm/s}$  and  $h_0 = 100\text{m}$  in the  $(y, z)$  plane at  $x=58.7\text{km}$ . Contour spacing =  $5 \times 10^{-3}\text{m/s}$

It is difficult to determine rigorously whether the isopycnal perturbations seen downstream of the ridges are hydraulic jumps. The flow would be hydraulically controlled at the top of the ridge if there is a transition from subcritical flow to supercritical flow. For steady, uniformly stratified flow Long (1953) determines the critical topographic height at which transitions will occur in terms of the mode number  $NH/U$ , where  $H$  is the total depth. However, our scenario is one of oscillating flow with non-uniform stratification. The initial perturbations to the isopycnals and the flow are confined to near the bottom topography because of the stratification, so it is unlikely that the total depth influences the formation of these jump-like features. Instead we make a local diagnosis: supercritical flow occurs when the horizontal flow speed exceeds the phase velocity of the internal wave, thereby preventing phase propagation in the horizontal direction. The phase velocity of waves in the alongslope direction is  $C_y = \omega/L$ . For  $L = 2\pi/\lambda$  and  $\omega = n\omega_0$ , this gives  $C_y = n \times 7.47\text{cm/s}$ . The maximum velocity in figure 15b is  $16.9\text{cm/s}$ . Even away from the ridges the peak flow is supercritical to waves of frequency  $\omega_0$  (since  $R_L > 1$ ), but locally over the ridge the peak flow is also supercritical to waves at frequency  $2\omega_0$ . At the height of the ridge in this location, the stratification is  $N = 6.99 \times 10^{-4}\text{s}^{-1}$ , so that waves with frequency up to  $4\omega_0$  are possible, and are indeed found higher up the water-column (figure 12), so the accelerated flow over the ridge is not supercritical to all possible internal waves at the topographic wavelength. The flow is supercritical however to the frequencies at which Bell predicts most of the internal wave energy. Another way to consider the effect of the topography on the flow is to note that for  $R_L > 1$ , the flow must take fluid up and over the ridge. Whether or not the ridge impedes the flow depends on energetic considerations - kinetic energy from the flow must be used to increase the potential energy by lifting up the fluid against the stratification - which can be expressed as a local Froude number criterion: If  $U_0/h_0N = Fr < 1$  where  $h_0$  is the ridge height, then the flow is impeded by the ridge. For  $U_0 = 0.1\text{m/s}$ , and  $N = 7 \times 10^{-4}\text{s}^{-1}$  this gives a critical ridge height of  $h_0 = 142\text{m}$  to impede the flow. So we expect  $U10h300$ , where  $h_0 = 300\text{m}$  to impede the flow, whereas  $U10h100$  does not have

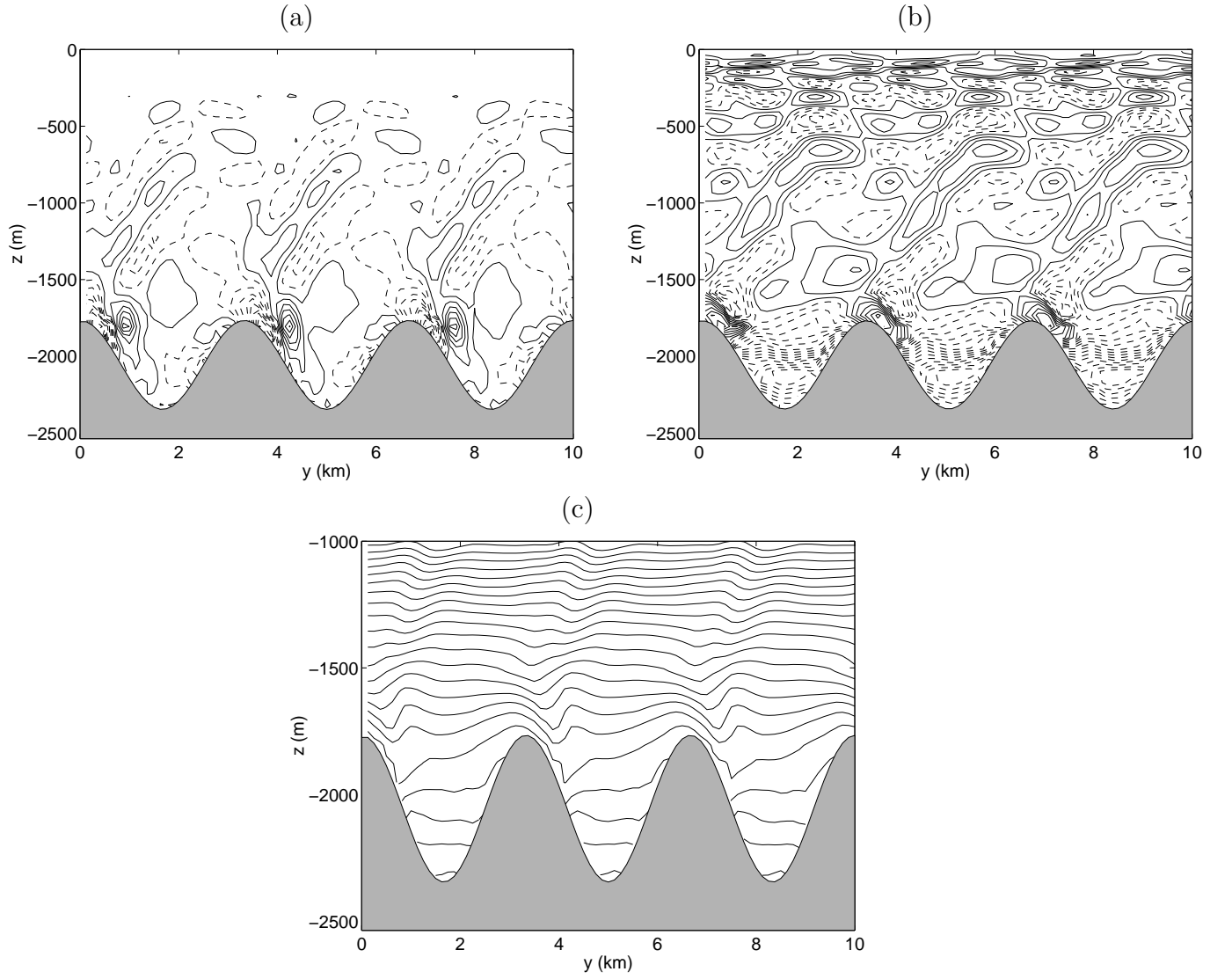


Figure 15: Instantaneous fields in the  $(y, z)$  plane at  $x=58.7\text{km}$  at a time  $t = 3.2T$  for  $U10h300$ ,  $U_0 = 10\text{cm/s}$  and  $h_0 = 300\text{m}$ : (a) vertical velocity, contour spacing  $5 \times 10^{-3}\text{m/s}$ , (b) alongslope velocity -  $10 \text{ cm/s}$ , contour spacing  $10^{-2}\text{m/s}$ , (c) buoyancy in the lower half of the domain, contour spacing  $3.9 \times 10^{-5}\text{m/s}^2$ .

sufficiently high ridges to block the flow. When  $U_0 = 0.02m/s$   $R_L < 1$ , so that flow is not forced up over the ridge. Hence a criterion for the possibility of hydraulic control might be  $R_L > 1$  combined with  $h_0 > U_0/N$ .

Time-depth plots of vertical velocity show little qualitative dependence on topographic height, and are largely influenced by the flow speed: time-depth plots for  $U2h300$  are very similar to those of  $U2h100$  and are therefore not shown. Figure 16 shows the time-depth plots for  $U10h300$ , with lines of constant phase overlain. In all plots, the vertical velocity patterns are mostly closely aligned with the  $3\omega_0$  line of constant phase, although close to the wall in figure 16a the  $4\omega_0$  line of constant phase might be closer.  $U10h100$  is similarly dominated by patterns aligned with  $3\omega_0$  lines of constant phase, and therefore not shown. Note that in the figure 16b the phase velocity in the stationary frame of reference is given by  $n\omega_0/L - U$ , where  $U$  is the advection speed, and we have used  $U = U_0$ . Whereas the inclusion of this advection correction made little difference for  $U_0 = 0.02$ , for  $U_0 = 0.1$ ,  $n = 1$  waves can no longer propagate in the alongslope direction, and the propagation speeds of the  $n = 2$  and  $n = 3$  waves are reduced significantly.

### 3.4 Mixing

These simulations do not reach a steady state, so it is difficult to say much about the transfer of energy between barotropic and baroclinic flow, or about the fraction of that energy which is dissipated versus that which is used for mixing. Within the short time-frame of the simulations, the net changes in tidally averaged stratification are small compared to the perturbations in stratification induced by the waves. The largest changes in stratification are found near the surface where stratification is reduced right adjacent to the surface, and increased just below, perhaps indicating mixing when the reflection of waves from the surface occurs. However, the signal to noise ratio is small (given the large amplitude of wave temperature perturbations in the strongly stratified near surface layer), so this is not a robust result. Another region of stratification changes is at depth (figure 17). Stratification is eroded within the valleys, and enhanced above the ridges. In  $U10h300$  the erosion of stratification might be associated with the hydraulic jumps, but again, the signal to noise ratio is small.

## 4 Discussion and conclusions

We have described a series of calculations of the internal waves generated by barotropic tide flow along a corrugated slope, examining the influence of the shape of the background slope, the stratification profile, and the amplitude of the barotropic flow and corrugations. In all the calculations with moderate forcing amplitude we find a response with a frequency twice that of the forcing (as indicated by spectra and phase propagation), whereas theoretical predictions are for a response at the forcing frequency. The upper part of the concave slope is supercritical to waves of the forcing frequency, but subcritical to waves of  $2\omega_0$  over all but the steepest section. We find that as a result of the largely subcritical slope, the nonlinear stratification has a far greater influence on the response than the shape of the slope (concave versus linear). For uniform stratification a quasi-modal pattern is established away from the bottom topography, with no phase propagation in the vertical

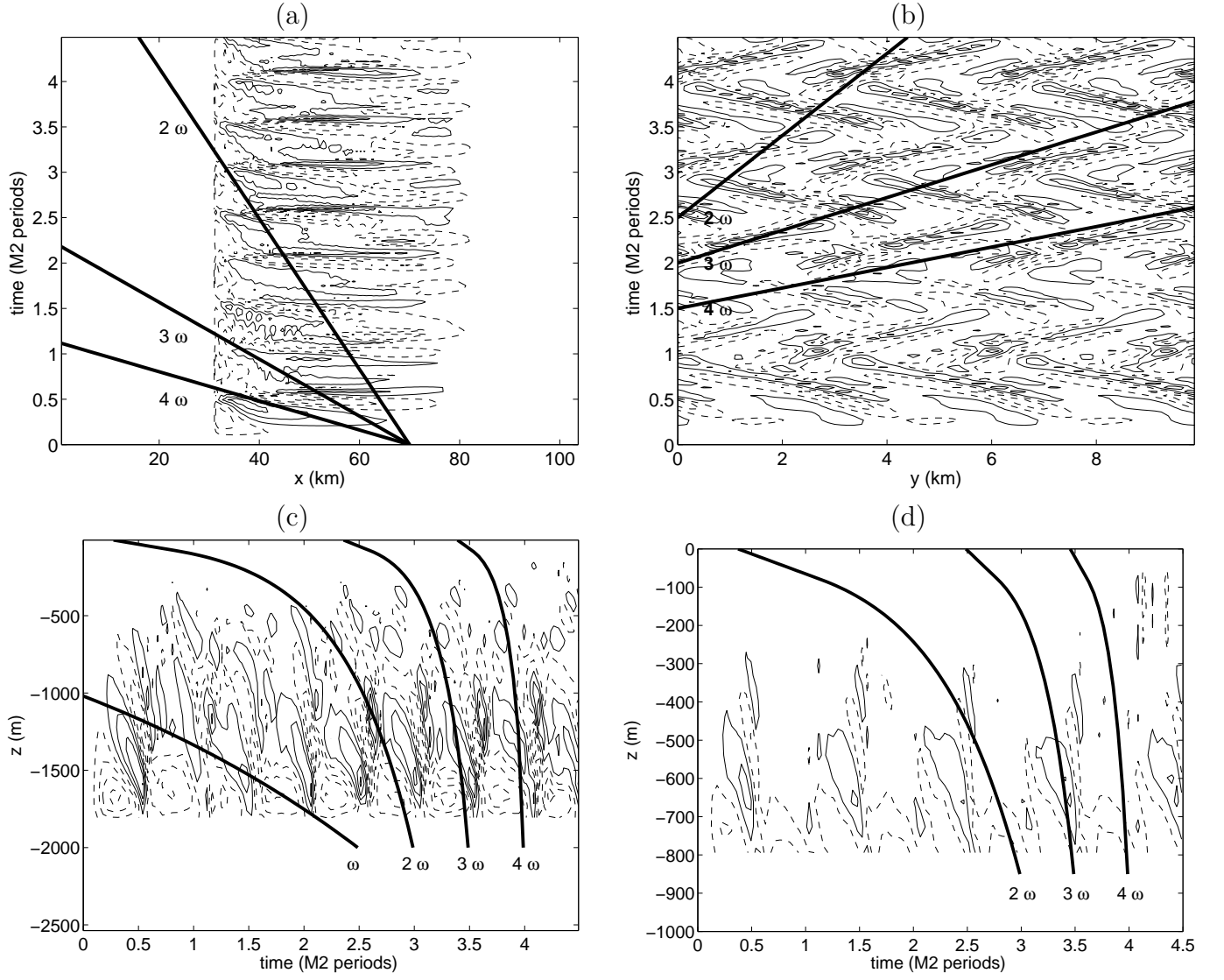


Figure 16: As for figure 6 but for  $U10h300$ . Contour spacing is  $5 \times 10^{-3} m/s$ . Lines of constant phase are shown for waves of frequencies  $\omega_0$ ,  $2\omega_0$ ,  $3\omega_0$ , and  $4\omega_0$ . In (a) and (d) the slope is supercritical to the fundamental frequency, so only the higher harmonics are shown.

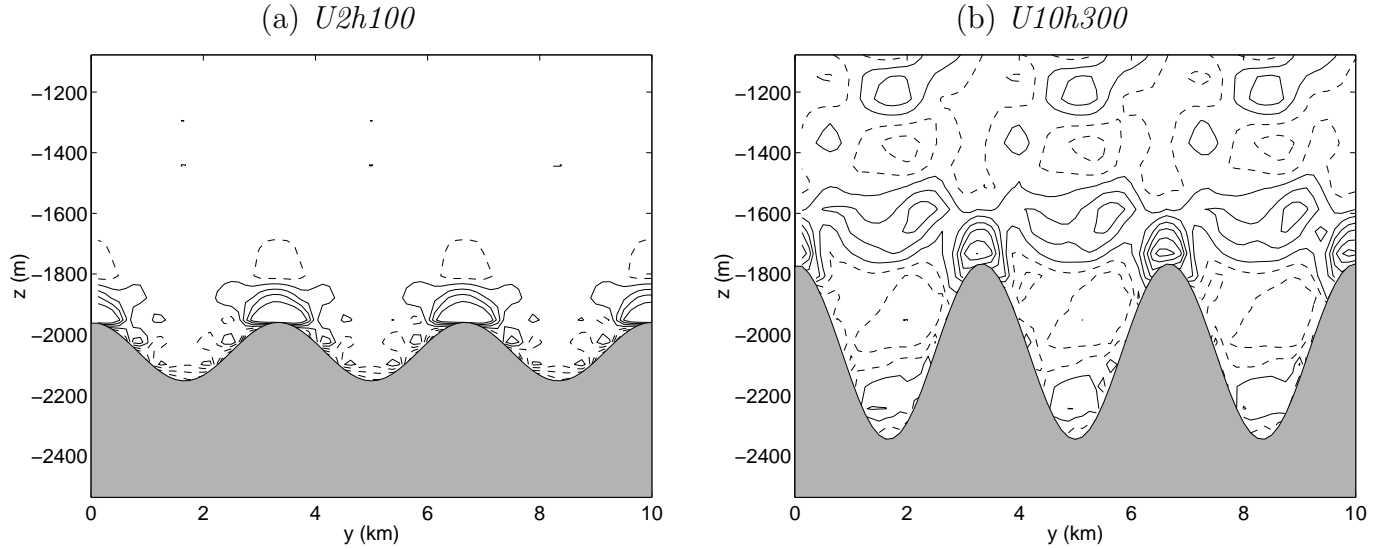


Figure 17: The change in stratification  $\Delta N^2$  over the length of the calculation, for the two cases *U2h100* and *U10h300*. This stratification change is the difference between the stratification of the initial state, and the stratification averaged over the final tidal cycle. Contour spacing: (a)  $2 \times 10^{-8} s^{-2}$ , (b)  $6 \times 10^{-8} s^{-2}$ .

nor in the along-slope direction. By contrast the nonuniform stratification cases all have downward phase propagation (upward energy propagation), indicating an absence of downward reflected waves. The timescale for waves to propagate and reflect from the top surface is considerably longer in the nonuniform stratification cases than for the uniform stratification, and perhaps after several reflections similar modal behavior might appear in the non-uniformly stratified runs too. Alternatively there might be dissipation of the waves in the thermocline (hinted at by possible decreases in stratification near the surface). Longer simulations would be necessary to clarify the behavior at steady-state.

When the flow speed is increased, more harmonics are seen in the response. The relative amplitude of the higher harmonics is greater than predicted from linear theory. In particular, when large flow speed is combined with large amplitude corrugations, structures which may be internal hydraulic jumps are observed downstream of the ridges. On relaxation of the flow, these propagate upward and in the along slope direction as internal wave packets with many higher frequency components appearing. These are probably a deep water equivalent of the solitary wave packets observed propagating onto the shelf every tidal cycle (MacKinnon and Greg, 2002).

The corrugation amplitude affects the energy levels relatively little, compared with estimates from linear theory (Bell, 1975a,b). This would support results from Li (2003) and Khatiwala (2003), indicating a saturation in internal wave energy levels for sinusoidal steep topography (recalling that even our “low amplitude” corrugations have steepness  $\epsilon_y > 1$ ).

These simulations suggest two possible mechanisms for mixing by the flow of barotropic tide over a corrugated slope. First, in the valleys of the corrugations, mixing may occur due to internal

hydraulic jumps. This occurs only for large amplitude corrugations and large amplitude forcing, with the criterion that the accelerated flow speed over the topography exceeds the phase speed of the dominant harmonic generated at the topography for hydraulic control to occur, i.e.

$$U^* > \frac{n\omega_0}{L} \quad (9)$$

where  $U^*$  is the enhanced flow over the ridge (which will increase as  $h_0$  and  $U_0$  are increased), and  $L$  is the corrugation wavenumber. Since  $n$ , the preferred harmonic, increases as  $U_0 L / \omega_0$  increases, we can equivalently state that  $U^* / U_0$  must be large for hydraulic control to occur. In addition, a necessary condition for hydraulic control is that the flow is impeded by the ridge, so that  $U_0 / (h_0 N) = Fr < 1$ , combined with  $R_L > 1$ . Note that  $Fr$  can be expressed as a combination of the nondimensional parameters  $R_L$  and  $\epsilon_y$ :

$$Fr = \frac{R_L}{\epsilon_y} \frac{\omega}{Ns} \quad (10)$$

So small  $Fr$  combined with large  $R_L$  implies large  $\epsilon_y$ , i.e. steep slopes. We would expect hydraulic control to be a possible mechanism for mixing whenever large amplitude flow is accelerated over large topographic perturbations. Note that such scenarios are excluded from Bell's theory by the assumption of small amplitude topography.

Secondly, a possible dissipation of wave energy in the thermocline for nonlinear stratification hints at possible mixing in the thermocline. Note that although vertical velocities are small in the thermocline, horizontal velocities are large, and shear instability could result. However in these simulations, shear instability was not directly observed in the thermocline, at least over the relatively short timescale of the simulations, and energy was probably dissipated by model viscosity and implicit numerical diffusivity.

In comparison with the observations, we have principally identified responses at frequencies which the observations did not sample. Observations identified mixing above the corrugations. The observed flow speeds and corrugation amplitudes are closest to those of  $U2h100$  however, where little reduction in stratification is seen. We have to conclude therefore that the alongslope barotropic forcing is not likely to be responsible for the observed mixing in the TWIST region. However, internal hydraulic jumps associated with along-slope barotropic tidal flow over ridges have been observed in other regions (e.g. Nash and Moum, 2001) and it is likely these results are applicable elsewhere.

These simulations have shown a response which is at higher frequencies than predicted from existing theory. A possible explanation for this higher frequency response might be that finite acceleration of the flow occurs over the ridges, not included in Bell's theory, so that the actual effective forcing velocity is increased. This is an avenue for future research, and suggests that observations of tidally generated baroclinic motion need to examine higher frequency flow components. Finally it should be noted that in our previous paper (Legg, 2003) describing the baroclinic response to cross-shelf forcing, the response was entirely at the fundamental frequency. This difference stems from the very different length scales of the slope/shelf break topography ( $O(50\text{km})$ ) compared to the corrugations ( $3.3\text{km}$ ).



# Acknowledgments

This work has been funded by ONR grant N00014-98-1-0096, with calculations carried out on NRL supercomputers. Discussions with Kurt Polzin, Samar Khatiwala, Jonas Nycander, Jonathan Nash, Ray Schmitt and Carl Wunsch have all aided in the course of this study.

# References

- Baines, P.G., 1982: On internal tide generation models. *Deep Sea Res.*, **29**, 307-338.
- Balmforth N.J., G.R. Ierley, W.R. Young, 2002: Tidal conversion by subcritical topography. *J. Phys. Oceanogr.*, **32**, 2900-2914.
- Bell, T.H., 1975a: Lee waves in stratified fluid with simple harmonic time dependence. *J. Fluid Mech.*, **67**, 705-722.
- Bell, T.H. 1975b: Topographically generated internal waves in the open ocean. *J. Geophys. Res.*, **80**, 320-327.
- Egbert, G.D. and R.D. Ray, 2000: Significant dissipation of tidal energy in the deep ocean inferred from satellite altimeter data. *Nature*, **405**, 775-778.
- Khatiwala, S. 2003: Generation of internal tides in an ocean of finite depth: analytical and numerical calculations. *Deep Sea Res.* **50**, 3-21.
- Ledwell J.L., E.T. Montgomery, K.L. Polzin, L.C. St Laurent, R.W. Schmitt and J. Toole, 2000: Evidence for enhanced mixing over rough topography in the abyssal ocean. *Nature*, **403**, 179-182.
- Legg, S., 2003: Internal tides generated on a corrugated continental slope. Part I: Cross-slope barotropic forcing. *J. Phys. Oceanogr.* submitted.
- Li, M., 2003: Energetics of internal tides radiated from deep-ocean topographic features. *J. Phys. Oceanogr.*, submitted.
- Marshall, J., A. Adcroft, C. Hill, L. Perelman, and C. Heisey, 1997. A finite-volume, incompressible Navier Stokes model for studies of the ocean on parallel computers. *J. Geophys. Res.*, **102**, 5753.
- MacKinnon, J.A., and M.C. Gregg, 2002: Mixing on the late-summer New England Shelf: Solibores and Stratification. *J. Geophys. Res.*, submitted.
- Nash, J.D. and J.N. Moum, 2001: Internal hydraulic flows on the continental shelf; high drag states over a small bank. *J. Geophys. Res.*, **106**, 4593-4611.

- Nash, J.D., E. Kunze, J.M. Toole, R.W.Schmitt, 2003: Internal tide reflection and turbulent mixing on the continental slope. *J. Phys. Oceanogr.*, submitted.
- St Laurent, L., S. Stringer, and Chris Garrett, 2003: The generation of internal tides at abrupt topography. in press in *Deep Sea Res.*.
- Thorpe, 1992: The generation of internal waves by flow over the rough topography of a continental slope. *Proc. Roy. Soc. London, Ser. A*, **439** 115-130.
- Thorpe, S.A., 1996: The cross-slope transport of momentum by internal waves generated by alongslope currents over topography. *J. Phys. Oceanogr.*, **26**, 191-204.